

# Multiresolution Phase Portrait Analysis for Segmentation of Ultrasound Images for Detection of Breast Cancer

Sirikan Chucherd and Stanislav S. Makhanov

**Abstract**—Computer aided diagnostics of early stages of the breast cancer is one of the most challenging problems of the contemporary medical image processing. Computerized detection of the breast tumors from ultrasound images provides the way which helps the physicians to decide whether a certain solid tumor is benign or malignant. However, it is one of the most difficult types of images to assess.

We propose a new method to improve the accuracy of the tumor detection based on phase portrait method combined with the multiresolution analysis. This approach is used as a pre-processing procedure followed by the generalized gradient vector flow field and detection by active contours (snakes). We analyze our approach with the synthetic images and a series of the real ultrasound breast tumor images and compare the results with the ground truth hand-drawn by the radiologists. Our numerical experiments show that the proposed method over performs the conventional generalized gradient vector field endowed with classical preprocessing such as the Gaussian smoothing, median filtering, etc.

**Index Terms**—phase portrait analysis, multiresolution analysis, medical image processing

## I. INTRODUCTION

**A**CTIVE contours or snakes proposed by Kass et al. [1]. have been extensively used in computer vision and image processing for edge detection, image segmentation and motion tracking. In particular, they have been applied (with a different degree of success) to locate the object boundaries in various applications of medical image processing such as segmentation of abnormalities in the images of the human heart, liver, brain, breast, etc. [2], [3], [4], [5].

The most important component of the snake is an external force derived from the image gradient vector field which pushes the snake towards the boundary. However, the gradient created nearby the boundary (edge) must be extended so that the snake “feels” the object even if it is far from it. Therefore, a variety of modifications of Kass’s method enhance the effect of the image edges and overcome the sensitivity to the initial conditions and the noise. The balloon snakes [6], [7] introduce an external force which inflates or deflates the contour even though it might be far from the actual boundary.

The sectored snakes [8] evolve subject to constraints derived from a priori knowledge of the object so that the

snake converges to a contour having some features of the prescribed shape.

Zhu and Yuille [9] performed the snake based segmentation starting from multiple seeds by iterative boundary deformation and region merging.

One of the most popular modification are the gradient vector flow (GVF) snakes introduced by Prince and Xu [10], [11]. The GVF minimizes a certain variational functional derived from a gray level edge map computed from the image. It is designed to enhance the capture range, extend the large gradients far from the boundary and smooth the gradients caused by noise and speckles. The resulting Euler equation are similar to steady state linear diffusion model.

Prince and Xu extended the GVF to the generalized gradient vector field (GGVF) [12] by introducing non-linear diffusion.

The GGVF based techniques have numerous applications in medical image processing (see for instances survey [13]). Examples of using GGVF for ultrasound (US) imagery are [14], [15], [16], [17], computed tomography images [18], mammography images [19], magnetic resonance imaging [20].

However, the GGVF treatment of the ultrasound images is still far from perfect. Although the GGVF is able to smooth false gradients created by tissues, shadows and random noise, in many cases it produces false boundaries and artifacts. On the other hand an excessive smoothing destroys the actual boundary and the accuracy of resulting contour becomes unacceptable.

This paper presents a numerical treatment of the GGVF images to improve the accuracy and convergence of the GGVF snake. Our modification called the phase portrait force field analysis (PPA) is inspired by discrete force field analysis [21]. The algorithm finds patterns resembling standard linear flow configurations and classifies them as the noise, the boundary of an object or the regular point.

We use the standard linear flow classification shown in Fig.1 and convert it into the image processing terms. The boundary is represented by the node-saddle. The noise is represented by an attracting star, repelling star, attracting node and repelling node(Fig.1).

It should be noted that in the past PPA has been applied to a variety image processing applications such as, satellite imagery [22], texture analysis [23], and the fingerprint identification [24]. In medical image processing PPA has been applied to detect abnormalities in mammogram breast tumor images [25]. However, to the best of our knowledge, the idea of PPA in the context of multiresolution GGVF active contours has been overlooked.

Manuscript received December 28, 2010; revised January 13, 2011. This work is sponsored by Thailand Research Fund grant BRG 5380016

S. Chucherd and S.S. Makhanov are with the School of Information, Computer and Communication Technology, Sirindhorn International Institute of Technology, Thammasat University, Bangkadi Campus, Pathum Thani 12000, Thailand e-mail: sirikan.chucherd@studentmail.siiit.tu.ac.th and makhanov@siiit.tu.ac.th.

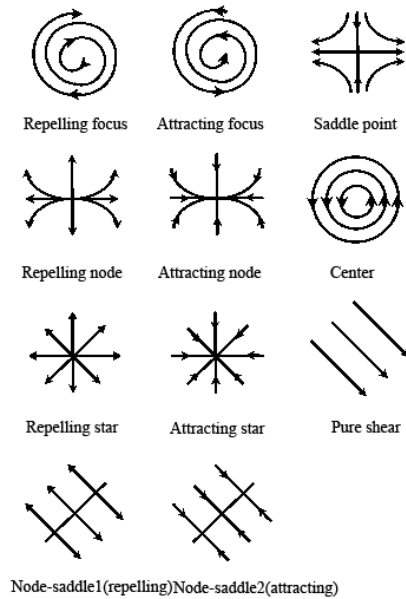


Fig. 1. Phase portrait flow pattern

As opposed to the majority of the phase portrait techniques based on “if-then” rules, we propose a continuous measure derived from the corresponding vector flow matrix.

The PPA applies to each multiresolution level, where the snake runs until convergence. The snake is then interpolated to the next level and the procedure repeats.

Our numerical experiments on numerous ultra-sound breast tumor images show a similar or better accuracy but at the same time much less sensitivity to the snake control parameters and the initial position of the contour as compared with the conventional GGVF, multiresolution GGVF snakes and multiresolution snakes endowed with conventional filters.

## II. BACKGROUND

### A. Snakes in the Framework of the Gradient Vector Flow Technique

An active contour or snake is a parametrically defined curve  $X(s) = (x(s), y(s))$ ,  $s \in [0, 1]$  which evolves inside the image domain so that it attaches itself to the desired object. The evolution of the snake is governed by Euler equations corresponding to an energy functional defined by

$$E = \int_0^1 \frac{1}{2} (a|X'(s)|^2 + b|X''(s)|^2) ds + \int_0^1 E_{ext}(X(s)) ds, \quad (1)$$

where  $E_{ext}$  is an external force which moves the snake towards the object. The minimum of the functional is supposed to be a curve which approximates a boundary of the object of interest. Although this claim has not been proven theoretically for realistic assumptions such as the presence of noise, false objects, speckles, low contrast areas, etc, a strong rationale behind it is variational functional(1).

Popular gradient vector flow techniques (GVF) originally proposed by Prince and Xu [10], [11], replace a “raw”

gradient vector field  $E_{ext}(X(s))$  derived from the image edges by a new vector field. The vector field is obtained by extending the large gradients at the boundary and smoothing gradients caused by noise. The GVF is a minimizer of the following functional

$$\mu \iint |\nabla u|^2 + |\nabla v|^2 dx dy + \iint |\nabla f|^2 |V - \nabla f|^2 dx dy, \quad (2)$$

where  $\mu$  is the diffusion coefficient.

The first integral produces a smoothly varying vector field  $V = (u(x, y), v(x, y))$ , while the second integral encourages the vector field to approach  $\nabla f$ , if  $|\nabla f|$  is large.

The Euler equation for functional(2) is given by

$$\mu \nabla^2 V - (V - \nabla f) |\nabla f|^2 = 0. \quad (3)$$

Equation(3) can be solved by treating  $V$  as a function of time and replacing (3) by :

$$\frac{\partial V}{\partial t} = \mu \nabla^2 V - (V - \nabla f) |\nabla f|^2. \quad (4)$$

The steady-state solution (as  $t \rightarrow \infty$ ) of the linear parabolic equation above is the desired solution of the Euler equation (3). Equation (4) is discretized with regard to the time and space variables and solved numerically. The time steps are interpreted as numerical iterations.

Xu and Prince [12] extended the GVF technique by introducing spatially varying coefficients to decrease the smoothing effect at the boundary, namely,

$$\frac{\partial V}{\partial t} - g(|\nabla f|) \nabla^2 V - h(|\nabla f|) (\nabla f - V) = 0. \quad (5)$$

The improved version of the GVF is called the generalized gradient vector flow (GGVF). The weighting functions  $g$  and  $h$  depend on the gradient of the edge map so that in the proximity of large gradients  $g$  gets smaller whereas  $h$  becomes larger. In [12] the following weighting functions have been proposed

$$g(|\nabla f|) = e^{-|\nabla f|/K}, \quad h(|\nabla f|) = 1 - g(|\nabla f|), \quad (6)$$

where  $K$  is a calibration parameter.

However, the GGVF may produce a vector field, where the gradients are not extended far enough from the actual boundary of the object. On the other hand, the true boundary can be partially or even entirely destroyed by excessive smoothing when  $K$  is too large.

The smoothing effect depends on the diffusion coefficient  $\mu$  (or  $K$  in case of (6)) and the iteration step. If a conventional stopping criteria based on the proximity to the steady state solution produces an “over-smoothed” solution, the user must modify the diffusion coefficient or interrupt the iterations earlier. However, interrupting the iterations too early may lead to false boundaries and artifacts.

The proposed PPA treats this problem by using local configurations of the vector field. If the local pattern resembles the noise the algorithm applies additional smoothing. If PPA detects a possible boundary the smoothing (diffusion) becomes small, so that this part of the vector field remains unchanged. Our experiments show that the same set of GGVF parameters achieves a better accuracy when PPA is applied. As a matter of fact, since PPA adapts the diffusion

TABLE I  
TYPES OF 2D CRITICAL POINTS.

Pattern	Eigenvalues	
Center	$R_1 = R_2 = 0$	$I_1 = -I_2 \neq 0$
Attracting Focus	$R_1 = R_2 < 0$	$I_1 = -I_2 \neq 0$
Repelling Focus	$R_1 = R_2 > 0$	$I_1 = -I_2 \neq 0$
Attracting Node	$R_1 \neq R_2 < 0$	$I_1 = I_2 = 0$
Attracting Star	$R_1 = R_2 < 0$	$I_1 = I_2 = 0$
Repelling Node	$R_1 \neq R_2 > 0$	$I_1 = I_2 = 0$
Repelling Star	$R_1 = R_2 > 0$	$I_1 = I_2 = 0$
Saddle Point	$R_1 > 0, R_2 < 0$	$I_1 = I_2 = 0$
Node-Saddle 1	$R_1 > 0, R_2 = 0$	$I_1 = I_2 = 0$
Node-Saddle 2	$R_1 < 0, R_2 = 0$	$I_1 = I_2 = 0$
Pure Shear	$R_1 = R_2 = 0$	$I_1 = I_2 = 0$

automatically, it is often the case that the dependence of the accuracy on  $K$  is substantially reduced.

### B. Phase portrait analysis

The phase portrait analysis makes it possible to introduce a continuous measure indicating the boundary point, regular point or noise based on the eigenvalues of the linear flow matrix [26]. The method applies to any size of the sampling window and works well combined with GGVF iterations.

There are eleven basic linear flow patterns characterized by the eigenvalues of the flow matrix (see Table 1, where  $\lambda_1, \lambda_2$  are the eigenvalues,  $R_i = \text{Re}\lambda_i$ ,  $I_i = \text{Im}\lambda_i$ ). Since we apply our classification to the vector field subjected to smoothing and boundary enhancing effects of GGVF. The most prominent patterns are attracting/repelling stars (noise), node-saddle (boundary) and the pure share (regular point).

Consequently, our classifier is given by

$$C(W) = \begin{cases} \text{noise, } \frac{\min(|\lambda_1|, |\lambda_2|)}{\max(|\lambda_1|, |\lambda_2|)} > \Delta_1, \\ \quad |\lambda_1| > \Delta_2 \text{ or } |\lambda_2| > \Delta_2 \\ \text{boundary, } \frac{\min(|\lambda_1|, |\lambda_2|)}{\max(|\lambda_1|, |\lambda_2|)} \leq \Delta_1, \\ \quad |\lambda_1| > \Delta_2 \text{ or } |\lambda_2| > \Delta_2 \\ \text{regular point,} \\ \quad |\lambda_1| \leq \Delta_2 \text{ or } |\lambda_2| \leq \Delta_2, \end{cases} \quad (7)$$

where  $W$  is the window around the pixel and  $\Delta_1, \Delta_2$  the thresholds evaluated by training.

### III. ITERATIVE ALGORITHM

The proposed algorithm combines GGVF-PPA snake with the multiresolution analysis (MRA) based on the Daubechies wavelets D4 [27]. The PPA detects the noise and boundary points for each multiresolution level and for various size of the window. The first run of PPA detects and removes the noise. The gray level in the corresponding windows gets smoothed. The second run detects the boundary. If the point belongs to the boundary, the gray level in the central point gets increased. Then the gradient vector field  $\nabla f$  is reconstructed and GGVF applies to improve  $\nabla f$ . Finally, the snake runs on the resulting vector field until convergence and is interpolated to the higher level. The procedure is repeated until the highest resolution level is achieved. The steps of the algorithm are given below.

- 1) Apply MRA to the original image(2-3 levels).
- 2) Set the resolution level to the lowest one.
- 3) Apply the Canny edge detector to obtain a gray level edge map.

- 4) Evaluate  $\nabla f$ .
- 5) Noise removal step:
  - a) Apply PPA with a certain window size to obtain  $C(W)$  at every point.
  - b) If  $C(W) = \text{"noise"}$ , smooth the gray level at this window(median filter, Gaussian filter, etc).
  - c) Increase the window size and go to 5.1 until the maximum window size is reached.
- 6) Evaluate new  $\nabla f$ .
- 7) Boundary detection step:
  - a) Apply PPA with a certain window size to obtain  $C(W)$  at every point.
  - b) If  $C(W) = \text{"boundary"}$ , increase the gray level of the edge map.
  - c) Increase the window size and go to 7.1 until the maximum window size is reached.
- 8) Evaluate new  $\nabla f$ .
- 9) Run GGVF on the improved vector field.
- 10) Run the snake on the final vector field until convergence.
- 11) Interpolate the snake to the next resolution level.
- 12) Set the image to the next resolution level.
- 13) Go to 3 until the highest resolution level is achieved.

In the boundary detection step, the gray level is increased by  $f_{new} = \alpha f_{old}$ , where  $\alpha$  is a prescribed coefficient. If  $f_{new} > 255$  at few points then  $f_{new} := 255$  but if  $f_{new} > 255$  at many points, the entire image is re-scaled. In our experiments  $\alpha = 1.5$ .

### IV. NUMERICAL RESULTS

Detection of tumors in the ultrasound (US) images by a trained physician is usually efficient and the number of false negatives is low. However, manual segmentation of the tumor boundary is tedious and time-consuming. Therefore, automatic segmentation techniques are important to help us to better visualize the tumor boundary, to calculate the volume of the tumor and to extract features needed for the tumor classification (benign or malignant).

This section presents experiments on real US images. The ground truth contours were outlined by Dr.Mavin Wongsaisuvan, who is currently a leading radiologist with the Queen Sirikit Center for Breast Cancer of King Chulalongkorn Memorial Hospital of Bangkok.

The proposed GGVF-MRA-PPA is compared with GGVF, GGVF-MRA and GGVF-MRA combined with the Gaussian smoothing (GS). The parameters of the algorithms are hand-tuned and the methods are compared when they perform the best (see similar evaluations in [13]).

The noise removal step uses the quantile filter [28]. It replaces intensities of all pixels in the sampling window by the minimal (in this window) gray level. The number of multiresolution levels is hand-tuned for the best performance.

The accuracy is evaluated in terms of the percentage of the true positives and the average Hausdorff distance between true contour and snake given by

$$\text{dist}_H(C_T, C_S) = \frac{\sum_{a \in C_T} \min_{b \in C_S} \frac{\|a-b\|}{N_T} + \sum_{a \in C_S} \min_{b \in C_T} \frac{\|a-b\|}{N_S}}{2}, \quad (8)$$

where  $N_T$  and  $N_S$  is the number of points belonging to the true contour and the snake respectively and  $|||$  denotes the Euclidean distance. The tables show the best accuracy from 50 GVF iterations performed for  $K = 0.01$  and  $K = 0.1$ (see equation (7)). The US images are shown in Fig. 2, 3 and 4.

Example 1. A low contrast malignant tumor. Complicated shape.

Consider a tumor shown in Fig.2. Let us analyze the performance of GGVF combined with different noise removal methods for varying diffusion coefficients (6). The snake has been initialized at an average Hausdorff distance of approximately 11, 17 and 22 pixels from the true boundary as follows. First, the snake is initialized inside a binary ground truth image which is “black” inside the tumor and “white” outside. Next, we let the snake grow until it reaches a prescribed distance from the boundary. Finally, we use this contour as the initial snake inside the real ultrasound image. The GGVF iterations are analyzed for extreme values of the diffusion coefficients:  $K = 0.01$  (slow diffusion) and  $K = 0.1$  (relatively high diffusion). The results in Table 2 and our forthcoming tables show the best accuracy vs. the distance between the snake and the true boundary from 50 GGVF iterations.

The best results of GGVF-MRA-GS and GGVF-MRA-PPA show a close accuracy when the snake is initialized at  $d = 11$  from the boundary. However, when the contour is initialized far from the boundary, GGVF-MRA-PPA outperforms GGVF-MRA-GS, GGVF-MRA and the conventional GGVF. For example, when the contour is initialized at 22 pixels from the true boundary, the best result produced GGVF-MRA-PPA for  $K = 0.1$  is by 20 percent better than that of GGVF-MRA-GS in terms of the true positive points. In turn, the Hausdorff distance is 5 times (!) smaller (Table 2). This is because the contours are different along a significant part of the boundary shown in Fig.2. For this experiment, number of multiresolution levels  $N_L = 3$ ,  $\Delta_1 = 0.81$ ,  $\Delta_2 = 0.1$  and the window size  $S_{max} = 15 \times 15$ .

Example 2. A low contrast malignant tumor. Complicated structure of the noise. A false boundary.

The image from Example 1 is characterized by an almost uniform background inside the tumor and a single large cluster of noise. This noise can be detected in one pass when the sampling window becomes large enough. As opposed to Example 1 the noise from Example 2 is much more complicated.

It includes several clusters scattered across the entire tumor. Some of the noise intensities are very close to the intensities of pixels from the true boundary. Such structures are hard to classify and eliminate. Besides, the tumor is characterized by a false boundary at the right side of the image(Fig.3(a)).

With these features the segmentation is intractable for conventional GGVF (Fig.3(c)). However, GGVF enhanced by MRA and subjected to a GS works much better. Figure 3 and Table 3 compare the performance of the proposed

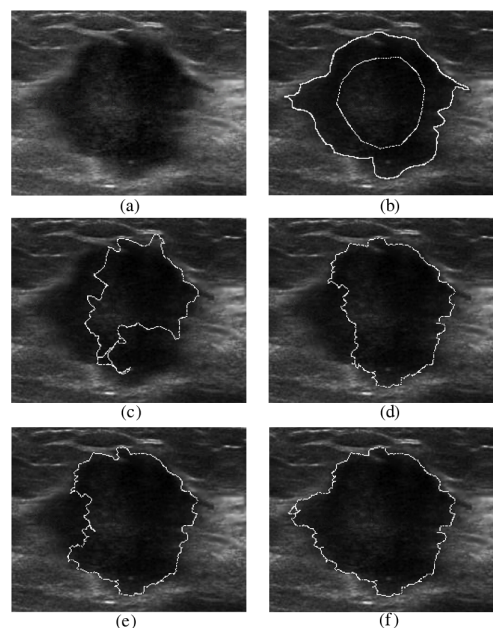


Fig. 2. Example 1. Low contrast US image, (782 × 616), ( $d = 22$ pixels). (a) The original image, (b) the initial contour and the ground truth, (c) GGVF, (d) GGVF-MRA, (e) GGVF-MRA-GS, (f) GGVF-MRA-PPA.

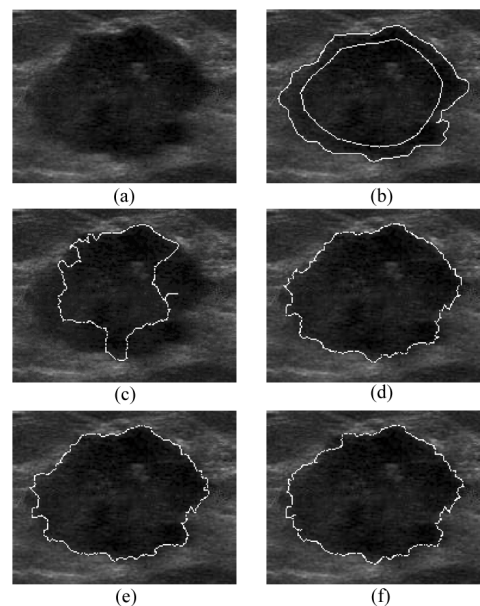


Fig. 3. Example 2. Low contrast US image, (687 × 535), ( $d = 12.6$ ). (a) The original image, (b) the initial contour and the ground truth, (c) GGVF, (d) GGVF-MRA, (e) GGVF-MRA-GS, (f) GGVF-MRA-PPA.

method with GGVF, GGVF-MRA and GGVF-MRA-GS. The accuracy is slightly different when the snake is initialized close to the boundary (at  $d = 6.8$  and  $d = 9.1$ ) for  $K = 0.1$ .

Furthermore, for  $d = 12.6$  the proposed method is better if  $K = 0.1$  (see Fig.3 (c)-(f)). It strongly outperforms other methods for  $K = 0.01$  (see Table 3). The good accuracy of

TABLE II

EXAMPLE 1. THE BEST ACCURACY(PERCENTAGE OF TRUE POSITIVES AND THE HAUSDORFF DISTANCE OF GGVF, GGVF-MRA, GGVF-MRA-GS, AND GGVF-MRA-PPA) VS. THE DISTANCE BETWEEN THE INITIAL CONTOUR AND THE TRUE BOUNDARY( $K = 0.01, K = 0.1, 50$  ITERATIONS).

$d$ (pixels)	GGVF		GGVF-MRA		GGVF-MRA-GS		GGVF-MRA-PPA	
	$K$		$K$		$K$		$K$	
	0.01	0.1	0.01	0.1	0.01	0.1	0.01	0.1
11.0	29.293	59.085	75.648	90.530	90.688	86.903	90.476	89.732
	7.873	3.755	3.820	1.624	1.142	1.737	1.545	1.494
17.4	20.027	42.154	55.177	89.715	64.151	87.132	89.808	90.075
	11.585	6.975	5.928	1.657	5.371	1.742	1.680	1.641
21.9	16.526	29.930	43.247	72.873	59.660	71.965	91.396	90.986
	19.224	18.289	12.432	8.237	12.199	6.600	1.690	1.441

GGVF-MRA-GS could be explained by smoothing effects of GGVF for large  $K$ . Nevertheless, large  $K$  is not always possible because strong diffusion may destroy the true boundary. It is much safer to run GGVF with small  $K$  and correct the noise by PPA. The local nature of PPA makes it possible to smooth only noisy areas while enhancing the boundary regions. For this experiment,  $N_L = 3, \Delta_1 = 0.85, \Delta_2 = 0.1$  and  $S_{max} = 10 \times 10$ .

Example 3. A low contrast benign tumor. High level of noise inside the tumor.

Consider a benign tumor depicted in Fig.4. The high level of noise disrupts the performance of GGVF and GGVF-MRA making them practically unacceptable.

As far as the GGVF-MRA-GS vs. GGVF-MRA-PPA is concerned, they perform equally well for  $K = 0.1$ . However, the results for  $K = 0.01$  are different again. The accuracy of GGVF-MRA-GS drops significantly for every  $d$ , whereas GGVF-MRA-PPA works relatively well. This exemplifies a typical case when small  $K$  is not able to suppress the noise (under-iterated GGVF). However, GGVF-MRA-PPA compensates for that by removing the noise from the tumor body. For this experiment,  $N_L = 2, \Delta_1 = 0.8, \Delta_2 = 0.1$  and  $S_{max} = 3 \times 3$ .

## V. CONCLUSION

The proposed combination GGVF-MRA-PPA applied to segmentation of the US tumor images of breast is capable of increasing the accuracy of the segmentation up to 5 times in terms of the average Hausdorff distance and up to 20% in terms of true positives. The method shows promising results when applied to the initial contour positioned far from the true boundary. Due to its local nature, the method works very well with the noise represented by a large group of pixels with the intensity different from the local background. The numerical experiments make it possible to conjecture that the proposed techniques will succeed in segmentation of a variety of tumors displayed in ultrasound images of the breast.

## REFERENCES

- [1] M. Kass, A. Witkin, and D. Terzopoulos, "Snakes: Active contour models," *International Journal of Computer Vision*, vol. 1, no. 4, pp. 321–331, 1988.
- [2] A. Evans and M. Nixon, "Biased motion-adaptive temporal filtering for speckle reduction in echocardiography," *IEEE Transactions on Medical Imaging*, vol. 15, no. 1, pp. 39–50, 1996.
- [3] F. Lefebvre, G. Berger, and P. Laugier, "Automatic detection of the boundary of the calcaneus from ultrasound parametric images using an active contour model: Clinical assessment," *IEEE Trans. Med. Imaging*, vol. 17, no. 1, pp. 45–52, 1998.
- [4] D. Chen, R. Chang, W. Wu, W. Moon, and W. Wu, "3-d breast ultrasound segmentation using active contour model," *Ultrasound in Med. and Biology*, vol. 29, no. 7, pp. 1017–1026, 2003.
- [5] M. Cvancarova, F. Albresgtsen, K. Brabrand, and E. Samsset, "Segmentation of ultrasound images of liver tumors applying snake algorithms and gvf," *Congress Series*, vol. 1281, pp. 218–223, 2005.
- [6] L. D. Cohen, "On active contour models and balloons," *Computer Vision, Graphics, and Image Processing. Image Understanding*, vol. 53, no. 2, pp. 211–218, 1991.
- [7] L. D. Cohen and I. Cohen, "Finite element methods for active contour models and balloons for 2d and 3d images," *IEEE Transactions on Pattern Analysis and Machine Intelligence*, vol. 15, pp. 1131–1147, 1991.
- [8] S. D. Fenster and J. R. Kender, "Sectorized snakes: Evaluating learned-energy segmentations," *IEEE Trans. Pattern Anal. Mach. Intell.*, vol. 23, no. 9, pp. 1028–1034, 2001.
- [9] S. C. Zhu and A. Yuille, "Region competition: Unifying snakes, region growing, and bayes/mdl for multiband image segmentation," *IEEE Transactions on Pattern Analysis and Machine Intelligence*, vol. 18, no. 9, pp. 884–900, 1996.
- [10] C. Xu and J. L. Prince, "Snakes, shapes, and gradient vector flow," *IEEE Transactions on Image Processing*, vol. 7, no. 3, pp. 359–369, 1998.
- [11] C. Xu and J. L. Prince, "Gradient vector flow: a new external force for snakes," in *Proceedings of the international IEEE Computer Society Conference on Computer Vision and Pattern Recognition*, 1997, pp. 66–71.

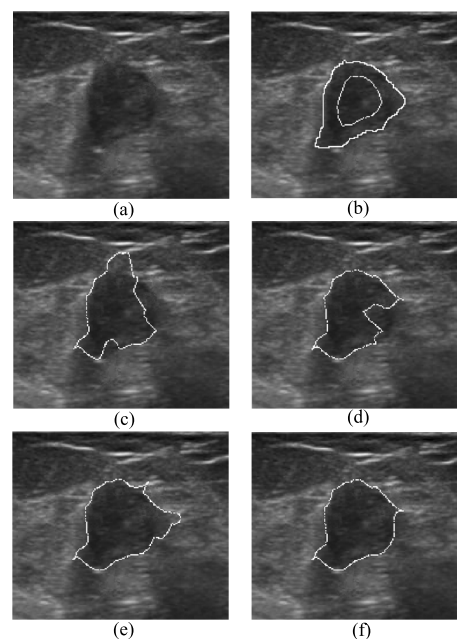


Fig. 4. Example 3. Low contrast US image, ( $500 \times 434$ ), ( $d = 12.2$ ). (a) The original image, (b) the initial contour and the ground truth, (c) GGVF, (d) GGVF-MRA, (e) GGVF-MRA-GS, (f) GGVF-MRA-PPA.

TABLE III

EXAMPLE 2. THE BEST ACCURACY VS. THE DISTANCE BETWEEN THE INITIAL CONTOUR AND THE TRUE BOUNDARY ( $K = 0.01, K = 0.1, 50$  ITERATIONS).

$d$ (pixels)	GGVF		GGVF-MRA		GGVF-MRA-GS		GGVF-MRA-PPA	
	$K$		$K$		$K$		$K$	
	0.01	0.1	0.01	0.1	0.01	0.1	0.01	0.1
6.8	59.678	65.605	79.266	85.259	82.154	83.960	85.003	85.230
	3.807	3.200	2.563	1.791	2.199	1.903	1.809	1.781
9.1	26.032	56.899	67.325	83.534	82.004	83.951	86.465	86.627
	9.058	3.998	3.146	1.956	2.144	2.012	1.741	1.690
12.6	12.185	22.179	26.460	75.960	36.137	77.688	68.379	80.738
	18.057	11.672	8.703	2.923	7.096	2.681	3.095	2.427

TABLE IV

EXAMPLE 2. THE BEST ACCURACY VS. THE DISTANCE BETWEEN THE INITIAL CONTOUR AND THE TRUE BOUNDARY ( $K = 0.01, K = 0.1, 50$  ITERATIONS).

$d$ (pixels)	GGVF		GGVF-MRA		GGVF-MRA-GS		GGVF-MRA-PPA	
	$K$		$K$		$K$		$K$	
	0.01	0.1	0.01	0.1	0.01	0.1	0.01	0.1
8.7	17.297	71.482	69.422	81.915	75.336	82.105	87.407	87.411
	8.037	3.126	3.970	2.144	3.423	2.125	1.945	1.942
10.8	11.364	68.932	33.714	82.230	59.193	81.915	87.732	87.266
	11.488	2.797	10.235	2.140	7.035	2.147	1.951	1.942
12.2	3.798	55.670	25.568	71.000	33.517	74.593	87.407	87.778
	12.868	4.735	11.472	3.435	10.573	2.276	1.949	1.954

- [12] C. Xu and J. L. Prince, "Generalized gradient vector flow external forces for active contours," *Signal Process.*, vol. 71, no. 2, pp. 131–139, 1998.
- [13] L. He, Z. Peng, B. Everding, X. Wang, C. Y. Han, K. L. Weiss, and W. G. Wee, "Review: A comparative study of deformable contour methods on medical image segmentation," *Image Vision Comput.*, vol. 26, no. 2, pp. 141–163, 2008.
- [14] M. Wei, Y. Zhou, and M. Wan, "A fast snake model based on non-linear diffusion for medical image segmentation," *Computerized Medical Imaging and Graphics*, vol. 28, no. 3, 2004.
- [15] J. Tang, "A multi-direction gvf snake for the segmentation of skin cancer images," *Pattern Recogn.*, vol. 42, pp. 1172–1179, June 2009.
- [16] X. Zhu, P. Zhang, J. Shao, Y. Cheng, Y. Zhang, and J. Bai, "A snake-based method for segmentation of intravascular ultrasound images and its in vivo validation," *Ultrasonics*, vol. 51, no. 2, pp. 181–189, 2010.
- [17] H. D. Cheng, J. Shan, W. Ju, Y. Guo, and L. Zhang, "Automated breast cancer detection and classification using ultrasound images: A survey," *Pattern Recognition*, vol. 43, no. 1, pp. 299–317, 2010.
- [18] G. Zhu, S. Zhang, Q. Zeng, and C. Wang, "Gradient vector flow active contours with prior directional information," *Pattern Recogn. Lett.*, vol. 31, pp. 845–856, July 2010.
- [19] F. Zou, Y. Zheng, Z. Zhou, and K. Agyepong, "Gradient vector flow fields and spiculated mass detection in digital mammography images," in *Proceedings of the 9th international workshop on Digital Mammography*, ser. IWDM '08. Berlin, Heidelberg: Springer-Verlag, 2008, pp. 299–306.
- [20] E. Vidholm, P. Sundqvist, and I. Nystrom, "Accelerating the computation of 3d gradient vector flow fields," *Pattern Recognition, International Conference on*, vol. 3, pp. 677–680, 2006.
- [21] Z. Hou and C. Han, "Force field analysis snake: an improved parametric active contour model," *Pattern Recognition Letters*, vol. 26, no. 5, pp. 513–526, 2005.
- [22] I. Cohen and I. Herlin, "A motion computation and interpretation framework for oceanographic satellite images," *Computer Vision, International Symposium on*, pp. 13–18, 1995.
- [23] X. Tian, S. Samarasinghe, and G. Murphy, "An integrated algorithm for detecting position and size of knots on logs using texture analysis," in *Proceedings of the Conference on Image and Visions Computing*, 1999, pp. 121–132.
- [24] J. Li, W.-Y. Yau, and H. Wang, "Constrained nonlinear models of fingerprint orientations with prediction," *Pattern Recogn.*, vol. 39, no. 1, pp. 102–114, 2006.
- [25] R. Rangayyan and F. Ayres, "Gabor filters and phase portraits for the detection of architectural distortion in mammograms," *Medical and Biological Engineering and Computing*, vol. 44, pp. 883–894, 2006.
- [26] D. Jordan and P. Smith, *Nonlinear ordinary differential equations : an introduction for scientists and engineers / D.W. Jordan and P. Smith*, 4th ed. Oxford ; New York : Oxford University Press, 2007, previous ed.: 1999.
- [27] I. Daubechies, *Ten Lectures on Wavelets*, ser. CBMS-NSF Reg. Conf. Series in Applied Math. SIAM, 1992.
- [28] A. Bengtsson and H. Bengtsson, "Microarray image analysis: background estimation using quantile and morphological filters," *BMC Bioinformatics*, vol. 7, p. 96, 2006.